International Journal of Greenhouse Gas Control xxx (2015) xxx–xxx

Contents lists available at ScienceDirect

International Journal of Greenhouse Gas Control

journal homepage: www.elsevier.com/locate/ijggc

Salt precipitation due to supercritical gas injection: I. Capillary-driven flow in unimodal sandstone

H. Ott [a,*], S.M. Roels [b], K. de Kloe [a]

[a] Shell Global Solutions International B.V., Kessler Park 1, 2288 GS Rijswijk, The Netherlands
[b] Department of Geotechnology, Delft University of Technology, 2628 CN Delft, The Netherlands

ARTICLE INFO

Article history:
Received 4 October 2014
Received in revised form 5 December 2014
Accepted 6 January 2015
Available online xxx

Keywords:
CO_2 storage
Dry-out
Precipitation
Counter-current flow
Micro-CT imaging
Sandstone

ABSTRACT

Drying and salt precipitation in geological formations can have serious consequences for upstream operations in terms of injectivity and productivity. Here we investigate the consequences of supercritical CO_2 injection in sandstones. The reported findings are directly relevant for CO_2 sequestration and acid–gas injection operations, but might also be of interest to a broader community dealing with drying and capillary phenomena.

By injecting dry supercritical CO_2 into brine-saturated sandstone, we investigate the drying process and the associated precipitation of salts in a capillary-pressure-dominated flow regime. Precipitation patterns were recorded during the drying process by means of μCT scanning. The experimental results and numerical simulations show that under a critical flow rate salt precipitates with an inhomogeneous spatial distribution because of brine and solutes being transported in counter-current flow upstream where salt eventually precipitates. A substantial impairment of the absolute permeability has been found, but despite high local salt accumulation, the effective CO_2 permeability increased during all experiments. This phenomenon is a result of the observed microscopic precipitation pattern and eventually the resulting $K(\phi)$ relationship.

The findings in this paper are related to unimodal sandstone. In a companion paper (Ott et al., 2014) we present data on the distinctly different consequences of salt precipitation in dual- or multi-porosity rocks.

1. Introduction

Drying of porous media is an important topic in many industrial processes, in soil science and for upstream operations such as gas injection and production into and from geological formation. Drying of saline formations will cause precipitation of salt initially dissolved in the brine. This can negatively affect the performance of injection and production wells and can even lead to well clogging, which is a serious risk for such operations. In this paper we consider large-scale geological storage of CO_2, originating from anthropogenic sources like fossil-fueled power plants or contaminated gas production, in order to reduce CO_2 emissions. Deep saline aquifers and depleted oil and gas fields are potential subsurface deposits for that purpose (IPCC, 2005; Bachu and Gunter, 2004).

If dry or under-saturated, supercritical (SC) CO_2 is injected into water-bearing geological formations like saline aquifers, water is removed either by viscous displacement of the aqueous phase or by evaporation/dissolution of water in CO_2 and subsequent advection in the injected CO_2-rich phase. Both mechanisms act in parallel, but while advection of the aqueous phase decreases with increasing CO_2 saturation (diminished mobility), evaporation becomes increasingly important as the aqueous phase becomes immobile. Below residual water saturation, only evaporation takes place and the formation dries out if no additional source of water is available. If water evaporates, the salts originally present in the water are left behind. In highly saline formations, the amount of salt that potentially precipitates per unit volume can be quite substantial. The volumes depend on brine salinity, and the transport of solutes and water in the reservoir. Since fluid saturations and flow rates close to the well bore cover a large range as functions of space and time, there are no easy answers to the questions whether, where and how salt precipitates and how precipitation affects injectivity. The questions that need to be addressed are about the mechanisms of solute

* corresponding author. Tel.: +31 70 447 3043.
E-mail address: Holger.Ott@Shell.com (H. Ott).

http://dx.doi.org/10.1016/j.ijggc.2015.01.005

transport on a macroscopic scale that determine the macroscopic distribution of salt, and the salt distribution on a pore scale that determines how the permeability is affected as function of porosity reduction.

Even though salt precipitation in the vicinity of gas production wells are generally considered as issue, there are not many studies published referring to well data. The frequently cited paper is that of Kleinitz et al. (2001). Probably due to the limited number of industrial-scale CO_2 sequestration projects, there are no well data available referring to salt precipitation during CO_2 injection.

The lack of well studies renders a proper problem statement difficult and we rely on numerical simulations and analytical models that are available in literature. Here, we only aim to highlight a few key studies on precipitation due to CO_2 injection relating to the problem discussed in this paper. In a series of publications, Pruess et al. presented numerical simulations of CO_2 injection in saline aquifers, investigating the fundamental aspects of formation dry-out and salt precipitation (Pruess and García, 2002; Pruess and Müller, 2009). The simulations were performed with a single injection well in idealized 1D and 2D radial geometries. The authors observed that precipitation occurs only in a narrow dry-out zone confined to a few meters around the injection well. The solid salt saturation in this zone has been found to be constant independent of the injection rate. 2D radial simulations were carried out to explore gravity effects. In contrast to the 1D-radial scenario, gravity in combination with capillary-driven flow lead to more heterogeneous precipitation, with a maximum observed solid-salt saturation of more than 20%.

Giorgis et al. (2007) performed field-scale simulation in radial geometry. The authors found that the amount of precipitate depends on brine mobility and can be high if there is a capillary-gradient driven brine flow in the direction of the well bore. The authors have further shown that the injection rate is an important factor in controlling precipitation process and in avoiding or allowing complete clogging of the formation. In their simulations, solid salt saturations of locally more than 60% have been reached.

However, field-scale simulations require input on flow physics and thermodynamics such as the $K(\phi)$ relationship and the mass transfer rates between the fluid phases. As we will show in this paper and in Ott et al. (2014), these parameters are of microscopic origin and need to be determined by laboratory experiments. The quality of the input is critical for reliable simulations as several studies suggest that a modest change in porosity might lead to a serious reduction in permeability. The respective literature is diverse in mechanisms and there are not many studies dealing with fluid-transport induced porosity changes. The discussed mechanisms range from the porosity variation due to lithology/rock type (Pape et al., 1999; Ehrenberg and Nadeau, 2005) via mechanical compaction (Wyble, 1958; Schutjens et al., 2004) to silica dissolution and precipitation in geothermal systems in single-phase flow (Xu et al., 2004b) to drying processes, i.e. in two-phase flow as discussed in the present paper. Even if usually described by power laws, it cannot be expected that the $K(\phi)$ relationships resulting from different mechanisms are comparable – i.e. process-independent – and generally applicable.

There are only a few studies on flow-through drying available, which are relevant for CO_2 storage. Zuluaga et al. investigated vaporization and salt precipitation in sand packs and sandstone for gas production wells (Zuluaga and Monsalve, 2001; Zuluaga et al., 2001). At the GHGT-10 in Amsterdam 2010, two experimental studies on dry CO_2 injection have been presented. The experiments have been performed in sandstone in realistic storage conditions addressing capillary-driven solute transport, the condition of counter current flow (Ott et al., 2011b), and a permeability porosity relationship (Bacci et al., 2011). Recently, Peyssona et al. (2014) and Andre et al. (2014) investigated the drying process by nitrogen injection in sandstone. The data have been used to benchmark a numerical simulation tool for field-scale modeling of CO_2 injection. Ott et al. (2011b) pointed out that modeling of vaporization by an equilibrium approach is not sufficient to describe core flood experiments. Roels et al. (2014) performed core flood experiments and succeeded in the description of the saturation profiles by a kinetic approach.

In this paper we show results of core-flood experiments that were presented at the SCA conference in Halifax and at the GHGT10 in Amsterdam in 2010 (Ott et al., 2010, 2011b). The experiments were performed to investigate the drying process and the impact of salt precipitation on flow, i.e. the salt distribution and the $K(\phi)$ relationship. For this we injected dry SC CO_2 in brine-saturated siliciclastic sandstone. The experiments were carried out at flow rates realistic for near-well-bore flow and at realistic thermodynamic conditions. During injection, spatial and time evolution of saturation changes were monitored by means of micro computed tomography (μCT). The results in this paper are based on a number of experiments showing precipitation profiles with different degrees of heterogeneity on a macroscopic scale. For quantification we discuss two of these experiments showing the largest and the smallest spatial variation of salt saturation after dry-out. We refer to the cases as the heterogeneous and the homogeneous case, respectively. We explain the mechanisms that lead to the observed heterogeneous distribution of the precipitate by means of numerical simulations.

In addition to the saturation profiles, changes in absolute permeability and effective CO_2 permeability were monitored. From this data, we extract the permeability/porosity relationship ($K(\phi)$). We explain the observed mild permeability reduction by the microscopic distribution of the salt with respect to the observed CO_2 flow channels. Furthermore, we discuss the results in terms of precipitation in single-phase and two-phase flow situations.

2. Materials and methods

The experiments were carried out in a core flood setup designed for flooding with volatile and reactive fluids as sketched in Fig. 1. A detailed description of the unit can be found elsewhere (Ott et al., 2012). In the following, only a brief description of the elements will be given that are of relevance for the experiments here presented.

The flow experiments were performed in vertical geometry, with fluids being injected from top to bottom. The samples were embedded in polycarbonate and placed in a carbon-fiber based core holder – both are materials with low X-ray attenuation coefficients. The core holder is placed in a μCT scanner for in situ 3D imaging of the rock-fluid system. CT imaging allows to determine fluid saturations and changes of the rock matrix due to salt precipitation. The unit is equipped with two feed sections for liquids and liquefied gas injection. The CO_2 feed pump was held at 3 °C during the experiments – liquid CO_2 was injected and heated to experimental temperature and to the respective SC state in the injection lines. The density difference has been taken into account for the indicated flow rates. From flow rates and the differential pressure measurement (ΔP), the absolute (K) and effective permeability ($K \times k_{rel}$) were derived on line.

The experiments were performed on Berea sandstone with an average permeability of 500 mD and 22% porosity. The samples were drilled from the same block and were small in cross section and volume (1 cm ø and 5 cm length) to obtain representative flow rates and to reduce the experimental time to complete dry-out. The mineralogy of Berea is dominated by quartz with some K-feldspar, kaolinite, and minor amounts of other clay minerals as determined by eSEM/EDX. The rock samples were pre-saturated with NaCl-based high-salinity brine: 20 wt% NaCl and 2 wt% CsCl.

Please cite this article in press as: Ott, H., et al., Salt precipitation due to supercritical gas injection: I. Capillary-driven flow in unimodal sandstone. Int. J. Greenhouse Gas Control (2015), http://dx.doi.org/10.1016/j.ijggc.2015.01.005

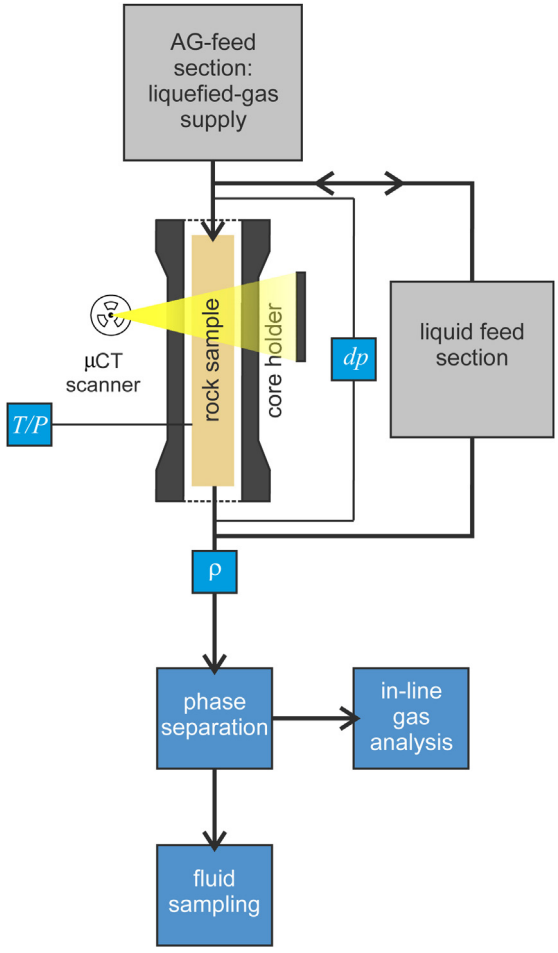

Fig. 1. Schematic of the experimental setup. More details are provided in Ott et al. (2012).

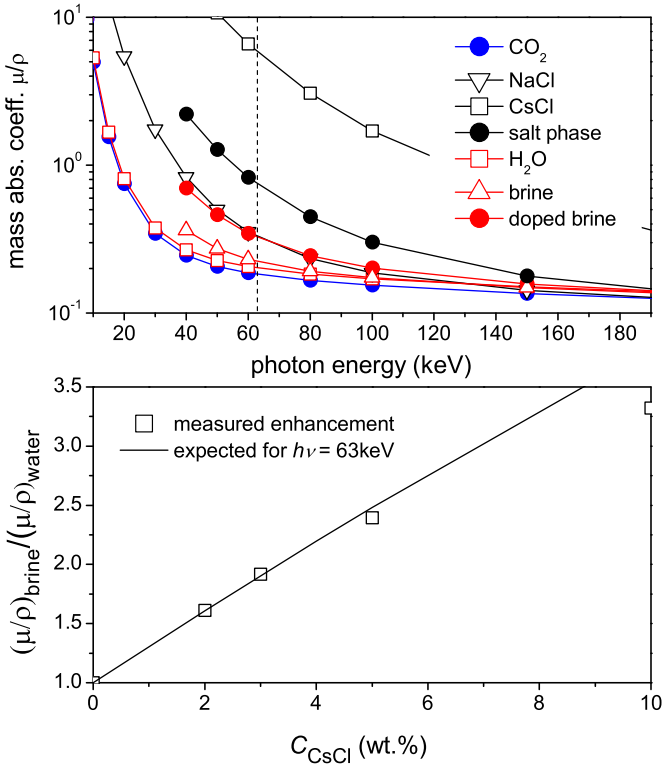

Fig. 2. Top: X-ray mass-absorption coefficients of the relevant fluids and salts as function of photon energy. The vertical line indicates the calibrated effective photon energy that has been used to calculate the salt saturation by Eq. (2). Bottom: relative absorption coefficients of the brine phase as function of CsCl concentration. The data has been used to determine the effective photon energy $h\nu = 63$ keV.

The CsCl was added as a contrast agent as its X-ray absorption coefficient is high, leading to a high X-ray absorption contrast in µCT between the aqueous and the CO_2-rich phase. The injected CO_2 was of high purity and essentially dry (strongly under-saturated with respect to water), not least because of the strong difference between water saturation limits at conditions in the lq.-CO_2 cylinder and at experimental condition of 100 bar pressure and 45 °C temperature.

We observe the spatial distribution of the precipitated-salt phase by means of µCT imaging. Computer tomography is based on X-ray absorption determined by material-specific linear attenuation coefficients (μ), which are directly represented as gray values of the voxels in the reconstructed image (Wellington and Vinegar, 1987; Vinegar and Wellington, 1987). For saturation calculations we made use of tabulated mass-absorption coefficients μ/ρ (Hubbell, 1969), fluid densities ρ (Pruess and Spycher, 2007; Span and Wagner, 1996), and the density of the solid-salt phase (Lide, 2003). μ/ρ for the injected and produced fluids and their constituents are shown in Fig. 2 and phase densities are listed in Table 1. Because of the sensitivity of saturation calculations to the X-ray-contrast agent, we measured relative absorption coefficients of CsCl solutions as a function of CsCl concentration. The curve is shown in the lower panel of Fig. 2; at 2 wt% CsCl, the mass-absorption coefficient is about 1.6 times larger than that of pure water. The CsCl calibration curve was also used to determine the effective photon energy of the µCT photon source ($h\nu_{eff} = 63$ keV) in order to derive the mass absorption coefficients used for the saturation calculations. The derived effective mass absorption coefficients are listed in Table 1.

Due to the higher solubility limit of CsCl, we expect that salt precipitates in a ratio different from the initial ratio $m_{NaCl}/m_{CsCl} = 10$, because CsCl might stay longer in solution and might be preferentially removed by the displacement process. To estimate CsCl depletion, we performed simulations (not shown) with the experimental brine composition. The simulations were performed as outlined in Section 4, but using ToughReact (Xu et al., 2004a) as simulation tool. NaCl and CsCl precipitations were handled in equilibrium using the ToughReact data base for NaCl and the CsCl-solubility data reported in Lide (2003). The simulations result in $m_{NaCl}/m_{CsCl} = 12.3$ and a respectively corrected scaling factor for saturation conversion according to Eq. (2).

3. Longitudinal precipitation profile

For each experiment a dry and clean rock sample was mounted into the core holder and subsequently pressurized and heated under N_2 flow to 45(±1) °C/100 bar (downstream side), corresponding to the thermodynamic conditions of a saline aquifer at a depth of about 1000 m. To quantitatively determine saturations, reference scans at 100% CO_2 saturation and 100% brine saturation were recorded. For that purpose, nitrogen was displaced by SC CO_2 (miscible displacement) until 100% CO_2 saturation was reached, as checked by the density of the produced fluid. Subsequently, the core was slowly depressurized and evacuated to allow brine saturation without trapping CO_2. The core was then saturated with brine and subsequently pressurized. All the reference scans were taken at experimental temperature and pressure. During the experiment, dry SC CO_2 was injected at a constant rate into the brine-saturated core. The injection rate at experimental condition was 2.2 ml/min

Please cite this article in press as: Ott, H., et al., Salt precipitation due to supercritical gas injection: I. Capillary-driven flow in unimodal sandstone. Int. J. Greenhouse Gas Control (2015), http://dx.doi.org/10.1016/j.ijggc.2015.01.005

Table 1
Densities at 100 bar and 45 °C and mass-attenuation coefficients for converting saturation profiles according to Eq. (2); * = dry, ** = water saturated, † = with, and †† = without CsCl, ‡ = in the presence of CO_2 ‡‡ = before CO_2-breakthrough. §: the deviation from the literature value can be explained by a ≈2K lower temperature in the external density meter.

	ρ_{CO_2} (kg/m^3)	ρ_{brine} (kg/m^3)	ρ_{salt} (kg/m^3)
Measured	585** → 565*,	1140†,‡‡ (±2)	–
Literature	499*, 517*,** (Spycher and Pruess, 2005)	1140††, 1172††,‡ (Spycher and Pruess, 2005)	2170 (NaCl), 3988 (CsCl), (Lide, 2003)
Used for saturation conversion	500	1140	2264 (m_{NaCl}/m_{CsCl} = 10) 2247 (m_{NaCl}/m_{CsCl} = 12.3)

	$(\mu/\rho)_{CO_2}$ (cm^2/g)	$(\mu/\rho)_{brine}$ (cm^2/g)	$(\mu/\rho)_{salt}$ (cm^2/g)
Used for saturation conversion	0.185	0.33	0.85 (m_{NaCl}/m_{CsCl} = 10) 0.75 (m_{NaCl}/m_{CsCl} = 12.3)

(later 4.4 ml/min) corresponding to realistic near-well-bore flow rates. During the first 40 min brine and CO_2 were produced and, in the following period, only a CO_2-rich phase with no further brine production. At that point, substantial drying by evaporation started, with a differential fluid pressure of about 600 mbar, decreasing to a lower final value of 460 mbar after about 8.5 h of CO_2 flooding as later discussed in Fig. 8.

Fig. 3 shows the integrated μCT-response profiles along the flow direction at different experimental time steps. The profiles are already converted to saturations by eliminating the rock matrix. The CO_2 saturation is represented with a scale ranging from 100% brine saturation ($S_{CO_2} = 0$) to 100% CO_2 saturation ($S_{CO_2} = 1$). The saturations have been calculated from integrated CT profiles $I(t)$ by:

$$S_{CO_2} = \frac{I_{brine} - I(t)}{I_{brine} - I_{CO_2}} \quad (1)$$

whereas I_{brine} and I_{CO_2} represent the density profiles of the reference scans at 100% brine and 100% CO_2 saturation, respectively. The first CT scan was started after 0.4 h of CO_2 flooding. The saturation profile is flat, with an average CO_2 saturation of about 0.5 (blue symbols). The displacement was still advection-dominated. Salt precipitation due to evaporation can be ignored and so the system was in a two-phase regime (CO_2-brine), for which S_{CO_2} is a good scale.

Subsequently the X-ray absorption decreases with time, in line with an increase in CO_2 saturation. If salt did not precipitate, flat density profiles would be expected, determined by the advection and evaporation of the brine phase. However, while the lightest component in this experiment (CO_2) was injected, a dip occurred at a position of about 2.5 mm, corresponding to a density increase – salt precipitates! The dip grew for about 9.5 h. After 10 h (red symbols) the shape of the profile, including all features, did not change further for another 6 h of CO_2 flooding. This is a clear indication that the sample is dry – no water evaporates and no salt is precipitating any more. We assume that at that point in time, the rock sample contained solid salt and CO_2, which again is a two-phase system. This allows the CT response for the red profile (dry state) to be rescaled to solid salt saturation by:

$$S_{salt} = (1 - S_{CO_2}) \cdot \frac{\mu_{brine} - \mu_{CO_2}}{\mu_{salt} - \mu_{CO_2}}, \quad (2)$$

where the μs denote the respective attenuation coefficients, derived from the mass-attenuation coefficients (μ/ρ) and the respective phase densities ρ, listed in Table 1, by $\mu = (\mu/\rho)\rho$.

The mean value of solid-salt saturation was determined as 4.1(±0.2)%.[1] However, locally the saturation is as high as 18%. The mean value of 4.1% corresponds to evaporation of 41(±2)% of the total water – the immobile water fraction. From this, the average degree of water saturation in the produced CO_2 has been estimated to be about 35(±2)% using the saturation limit of water in CO_2 (≈0.00145 wt.%, (Pruess and Spycher, 2007; Span and Wagner, 1996)), the injection rate and the experimental time to dry-out. From this we estimate the length scale of the evaporation zone to be in the order of 0.3–1 m, which evidently is controlled by evaporation kinetics and the flow rate of the CO_2-rich phase. A numerical estimation of the length of the evaporation zone will be given in Section 5.

The observed salt accumulation, which is locally much higher than the salt originally present in the brine in the same respective volume, is explained by a capillary-driven counter-current flow, as discussed further in the next section. However, after doubling the flow rate to 4.4 ml/min, a homogeneous precipitation pattern has been observed. Both precipitation patterns are shown in the lower panel of Fig. 3. An explanation of this effect will be given by

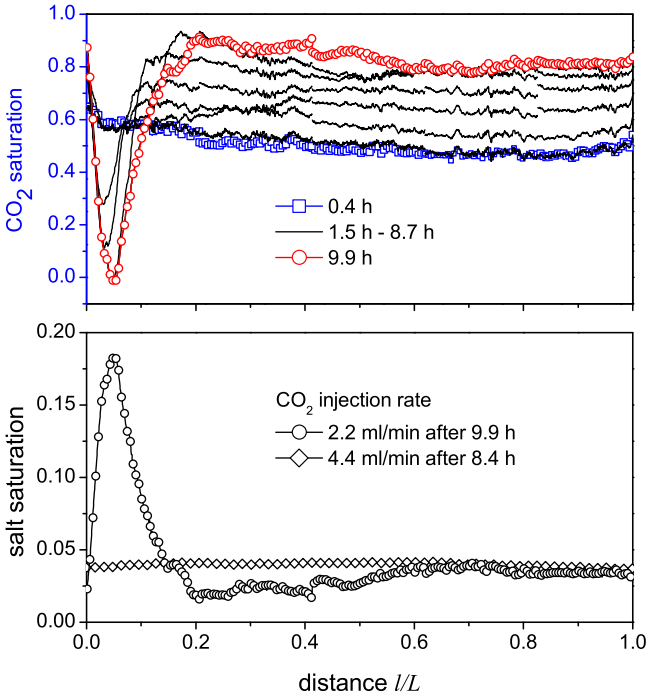

Fig. 3. μCT data recorded during the experiment. Top: Time series of normalized difference images projected onto the vertical sample axis in flow direction. The profiles represent changes of a three-phase system: brine/CO_2/salt. The saturation scales on the left and right correspond to the respective two-phase system at the beginning of the experiment and at the end: CO_2/brine and CO_2/salt, respectively.

[1] The saturation determination is mainly sensitive to the uncertainty in the dopant concentration, which might be affected by depletion as discussed in Section 2. The given errors result form the estimated error of the NaCl/CsCl ratio of (12.3) ± 1.

Please cite this article in press as: Ott, H., et al., Salt precipitation due to supercritical gas injection: I. Capillary-driven flow in unimodal sandstone. Int. J. Greenhouse Gas Control (2015), http://dx.doi.org/10.1016/j.ijggc.2015.01.005

numerical simulations in the next section. There it turns out that there is a critical flow rate above which salt precipitates homogeneously. It needs to be mentioned, that we did not observe a well defined critical flow rate, which is – as we believe – a result of the (relatively small) sample to sample variation of capillary properties. What we can state at this point is that the critical velocity for the given rock type and thermodynamic condition is in the range of the flow rates reported here.

4. Numerical modeling of the longitudinal profile

For an understanding of the fundamental mechanism behind the observed precipitation patterns, we performed numerical simulations with TOUGH2 (Pruess and Spycher, 2007), which is a multiphase/multi-component reservoir simulator. In combination with the fluid property module ECO2N that describes the thermodynamics of H_2O/NaCl/CO_2 systems, TOUGH2 has been used to model CO_2 injection in saline aquifers (Pruess and Spycher, 2007). The present experiments were modeled in a simple vertical 1D geometry using the experimental dimensions. The first grid block was assigned as the injection point at a constant CO_2-injection rate. The constant pressure boundary condition was realized by setting the volume factor of the last grid block to infinite. The rock-fluid properties K, k_{rel} and p_C were derived from experiments performed on the same rock type with the same fluid configuration (Perrin and Benson, 2010; Berg et al., 2013).[2]

The upper panel of Fig. 4 shows longitudinal CO_2-saturation profiles profile (in the direction of injection) simulated with a CO_2-injection rate of 3×10^{-5} kg/s for several time steps (black lines). At the given injection rate, the shock front passes the core within seconds, followed by a continuous saturation change after breakthrough. After about 0.3 h, a dip in the CO_2 saturation close to the injection point occurs. This is attributed to a saturation change due to salt precipitation as displayed in the lower panel. With advancing time, a precipitation front slowly moves from the injection point downstream, accumulating salt on its way. After 3.3 h of CO_2 flooding, the solid-salt saturation exceeds 0.9 and the simulation stops; in the next time step the salt saturation would reach 1. Permeability changes are not taken into account, but a blockage of pore space will obviously lead to clogging. At that point more salt is precipitated than was originally present in the respective brine volume, which requires transport of salt in the upstream direction to the point of dry-out, as also observed experimentally.

In the same panels in Fig. 4, simulations at higher and lower injection rates are displayed in their respective final states after dry-out. At higher injection rates the location of precipitation shifts away from the injection point toward a larger saturation gradient (as a result of the capillary end effect). Apparently, if the viscose force increases, a stronger saturation gradient is needed to reach the condition that leads to local precipitation. At lower flow rates, back flow seems to be even stronger, with the salt precipitating directly at the inlet with the time till clogging being longer.

More insight is provided by the fluid transport as displayed in Fig. 5. The effective water fluxes in individual cells at the point of local precipitation (closed symbols) and at the outlet (open symbols) are plotted against time. The streams are split into water flux in the CO_2-rich phase (blue circles) and in the aqueous phase

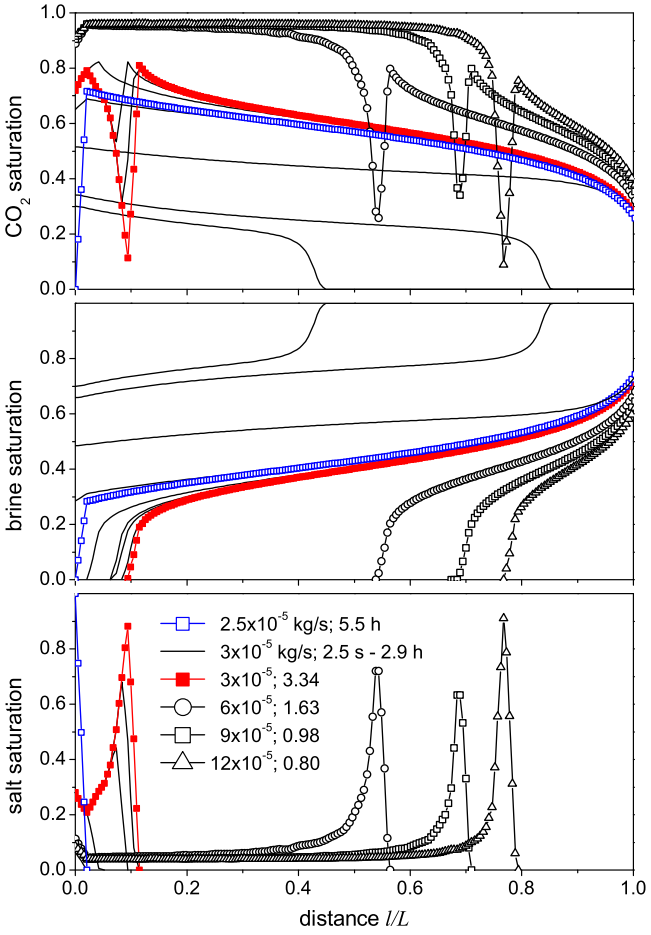

Fig. 4. TOUGH2 simulations of core-flood experiments. Upper panel: CO_2-saturation profiles during CO_2 injection into a brine-saturated rock sample at a rate of 3×10^{-5} kg/s and at different time steps (lines and filled squares). Also shown are the final states of simulations at higher injection rates as indicated in the figure (open symbols). The middle and lower panels show the respective brine and solid-salt saturation profiles.

(black squares). The red line marks the total water flux at the outlet. The water flux in the CO_2-rich phase is determined by the water content and the flow rate. It stays constant over a long period of time, according to the saturation limit. The water transport in the aqueous phase is very strong during the first few seconds but

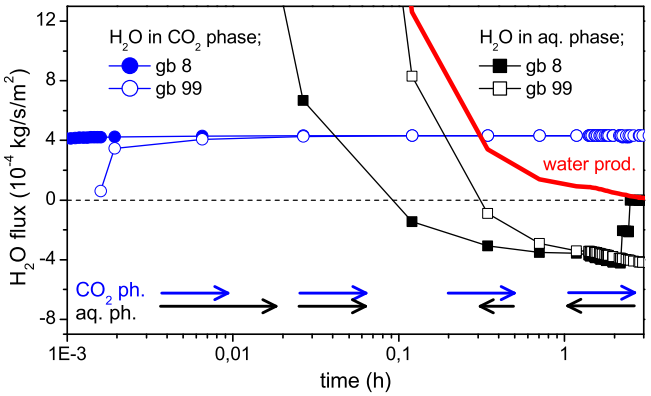

Fig. 5. H_2O fluxes in selected grid blocks (gb) as a function of time. Squares represent the H_2O flux in the aqueous phase and circles represent the H_2O flux in the CO_2-rich phase due to evaporation and subsequent advection. Note that the aqueous phase changes the flow direction as indicated by the arrows. (For interpretation of the references to color in text, the reader is referred to the web version of the article.)

[2] Experimental capillary pressure ($p_C(S_W)$) and relative permeability saturation functions ($k_r(S_W)$) were approximated by the van Genuchten models (van Genuchten, 1980) available in TOUGH2. We performed the simulations using the following parameter set: $\lambda = 0.48$, $S_{lr} = 0.079$, $S_{ls} = 1$, $1/P_0 = 3.5\times 10^{-4}$ and $P_{max} = 10^9$ for $p_C(S_W)$ and $\lambda = 0.7$, $S_{lr} = 0.15$, $S_{ls} = 1$ and $S_{gr} = 10^{-3}$) for $k_r(S_W)$. Furthermore, $K = 500$ mD, $P_{in} = 100$ bar, $T = 45\,^{\circ}$C (isothermal) and $X_{NaCl} = 0.24$ (initial brine salinity in wt%) were used.

Please cite this article in press as: Ott, H., et al., Salt precipitation due to supercritical gas injection: I. Capillary-driven flow in unimodal sandstone. Int. J. Greenhouse Gas Control (2015), http://dx.doi.org/10.1016/j.ijggc.2015.01.005

declines rapidly according to the mobility ratio of the fluid phases. The aqueous phase becomes immobile and the water transport is determined by evaporation and subsequent advection in the CO_2-rich phase. After a certain time, capillary pressure dominates the aqueous-phase transport, leading to a capillary-driven back flow into the zone of evaporation – counter current to the injected CO_2. Back flow, however, allows local accumulation of salt beyond the brine's original local salt content. The point at which the major part of the salt precipitates is the point at which the 'evaporation front' no longer moves. Here, the negative water flux in the brine phase compensates for the positive water flux in the CO_2-rich phase (see Fig. 5) and we can formulate a condition for local precipitation to occur if:

$$q_{SC} \cdot \rho_{SC} \cdot X_{H_2O,SC} = q_{aq} \cdot \rho_{aq} \cdot X_{H_2O,aq}, \quad (3)$$

where q_{SC} and q_{aq} are the volumetric fluxes of the CO_2-rich phase and the aqueous phase, ρ_{SC} and ρ_{aq} are the phase densities, and $X_{H_2O,SC}$ and $X_{H_2O,aq}$ are the mass fractions of water in both phases, respectively.

The simulations demonstrate and explain the effect observed in the experiment. However, there are substantial differences between experiments and simulations related to saturation gradients. In the simulation, the gradient is dominated by the capillary end-effect and is therefore a geometrical property. In the experiment, however, the end effect is suppressed (as observed in the CT profiles) by capillary back flow, i.e. capillary redistribution; in contrast to the simulation, water evaporates over the entire core length and, hence, the induced back flow equalizes the brine saturation, suppressing the end effect. This is a result of evaporation kinetics, which is not accounted for in the simulations with TOUGH2 (or in any other simulator which does not take evaporation kinetics into account). Hence the saturation gradient that leads to local precipitation is not quantitatively modeled. Second, there is only a finite brine volume in the experiment, due to the finite sample size. This leads potentially to an underestimation of salt saturation as a result of depletion effects in experiments with a finite volume, which can be shown by simulations with a finite sample volumes (data not shown here).

The critical flow rate, above which a homogeneous precipitation pattern is observed in the experiment (i.e. at which the advective flux prevents capillary-driven back flow), is equivalent to the rate in the simulations at which the precipitation peak moves away form the inlet to the next point with a higher saturation gradient were the downstream flux of water in CO_2 is again compensated by counter-current flow of the aqueous phase. Such a shift is not observed for the flat saturation profiles in the experiments, since the constant saturation gradient cannot counteract the advective force at flow rates above the critical. A flat saturation profile is expected in the field. However, in radial flow geometry, where the advective force decreases with distance, the condition of local precipitation can be reached at a certain distance even with a flow rate above the critical close to the injection point.

5. The zone of attraction: kinetic model

In the simulations presented so far the produced CO_2 was fully water-saturated as result of the equilibrium approach of the evaporation model. However, from the experiments in Section 3 we determined the average water saturation of the produced CO_2 stream to be about 35% of the solubility limit for the respective experimental conditions. The reason for the partial saturation is the finite contact area between the injected CO_2 stream and the brine in the rock and the finite evaporation rate, which is not taken into account (overestimated) in the equilibrium model. On the basis of the average water content of the produced CO_2, we

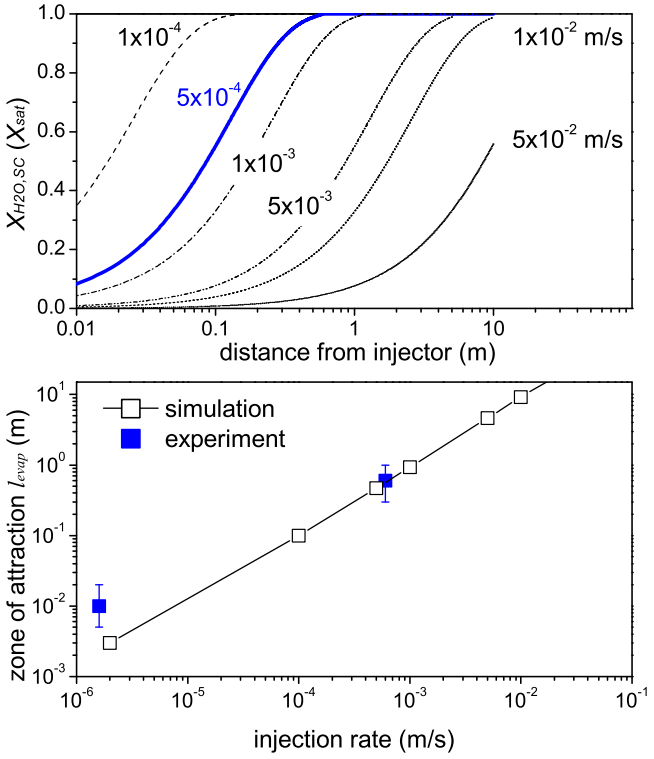

Fig. 6. Zone of potential attraction. Upper panel: Water saturation in the CO_2-rich phase as function of distance from the injection point. The profiles for different injection rates are shown simulated in a linear flow geometry. Lower panel: The zone of attraction as a function of injection rate. The filled symbols are obtained from experiments.

estimated the zone in which evaporation takes place to be in the order of 0.3–1 m in linear geometry – in any case longer than the experimental length scale. In this zone, the water saturation gradient (dS_W/dx) is modified from the gradient expected from viscous displacement only and capillary-driven back flow can occur. The evaporation zone is therefore the zone over which counter current solute transport can potentially occur – we therefore call it *zone of attraction*.

In this section we present an estimation of the zone dimension in linear geometry by numerical simulations. We use a kinetic approach as reported by Roels et al. (2014) and model the zone of attraction for different injection rates between 0.01 and 100 ml/min/cm^2 (2×10^{-6} and 0.1 m/s). We use rock-fluid parameters – relative permeability and capillary pressure saturation functions – obtained for CO_2-brine displacement in the same rock type (Berea sandstone: Ott et al., 2011a; Berg et al., 2013), for the same fluid combination and thermodynamic condition.

We model evaporation and flow only and we do not take the feedback of precipitation on permeability and capillarity into account. We determine the overall evaporation rate – $A \times r_{evap}$, with A being the CO_2-brine contact area and r_{evap} the evaporation rate – by matching the average water concentration in the produced CO_2 stream to the experimentally obtained value at the respective distance. Subsequently, simulations were performed with experimental input data on a semi-infinite simulation domain. From the simulation data we determined the distance, l_{evap}, over which evaporation takes place – i.e. the distance that is needed to reach water saturation limit in CO_2 under the respective conditions.

Fig. 6 shows the water saturation profiles in the CO_2 stream for different injection rates. Each simulation shows the typical increase of the water saturation in the CO_2 phase ($X_{H_2O,SC}$) with distance from the injector till equilibrium concentration (X_{sat}) is reached.

Please cite this article in press as: Ott, H., et al., Salt precipitation due to supercritical gas injection: I. Capillary-driven flow in unimodal sandstone. Int. J. Greenhouse Gas Control (2015), http://dx.doi.org/10.1016/j.ijggc.2015.01.005

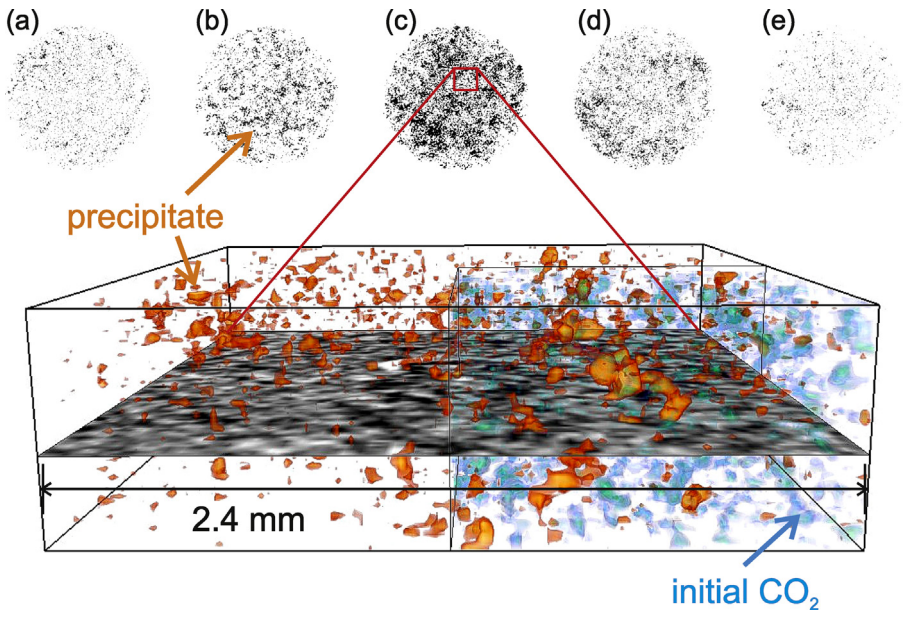

Fig. 7. μCT data recorded with pseudo pore-scale resolution during CO_2 flooding. Top row: cross-sectional difference images showing the solid salt saturation in the region of local precipitation between 0 and 0.5 cm from the inlet (image c at maximum salt saturation). Lower image: 3D representation of the salt distribution at 0.25 cm from the inlet (orange-red). The initial CO_2 percolation pattern (after 0.4 h) is added at the right front corner of the 3D volume.

The data show an increasing extend of the zone of attraction with increasing injection rate. The lower panel shows the derived l_{evap} as a function of CO_2 injection rate. The experimentally estimated data are included in the plot. For the defined range of injection rates, evaporation zones in the order of $l_{evap} = 3 \times 10^{-3}$ to above 10 m were found with a linear dependence on the injection rate. For the conditions at which the experiments were carried out, the zone of attraction has been simulated to be 0.4 m.

The presented kinetic simulations give valuable information about the size of the zone affected by salt precipitation and the distances over which solutes can be transported counter current in direction of the injector. This served the reservoir engineer as input for e.g. gridding of reservoir models around gas injectors and producers. The salt volume that potentially can be transported to the point of dry-out can be estimated from the immobile brine fraction in the respectively affected volume.

6. Effects on permeability: $K(\phi)$ relationship

Up to this point we have discussed the longitudinal solute transport and the resulting precipitation profiles. However, the important question is related to the effect of precipitation – i.e. porosity reduction – on permeability and eventually on injectivity. While porosity reduction is measured by μCT, changes of permeability are reflected in the pressure drop ΔP.

The upper panel of Fig. 8 shows the pressure drop over the core length during flooding (black line). ΔP essentially decreases during the experiment. The onset of capillary back flow is visible as a small dip, with a subsequent ΔP increase due to substantial local precipitation. But despite this porosity reduction, the effective permeability of the CO_2-rich phase increased during the experiment, which means that relative permeability effects compensate for the absolute permeability (K) reduction. A ΔP curve of a comparable experiment that showed a homogeneous precipitation pattern with about the same average porosity reduction is shown in the same plot (red line). The experiment was terminated after about 7 h and shows a smaller final reduction of K as in the heterogeneous case. From the final porosity profiles of both experiments as shown in Fig. 3 and the respective pressure drop, we determine a $K(\Phi)$ relationship for the dry state by using the correlation proposed by Verma and Pruess (1988):

$$\frac{K - K_C}{K_0 - K_C} = \left(\frac{\Phi - \Phi_C}{1 - \Phi_C}\right)^{\tau}, \tag{4}$$

with K_C being the lowest value to which K can be reduced by precipitation. While K_C is a robust outcome, the exponent τ and the critical porosity Φ_C are not uniquely defined by the data set alone. However, the two extremes, $\Phi_C = 0$ and $\Phi_C = 0.8$, give similar results

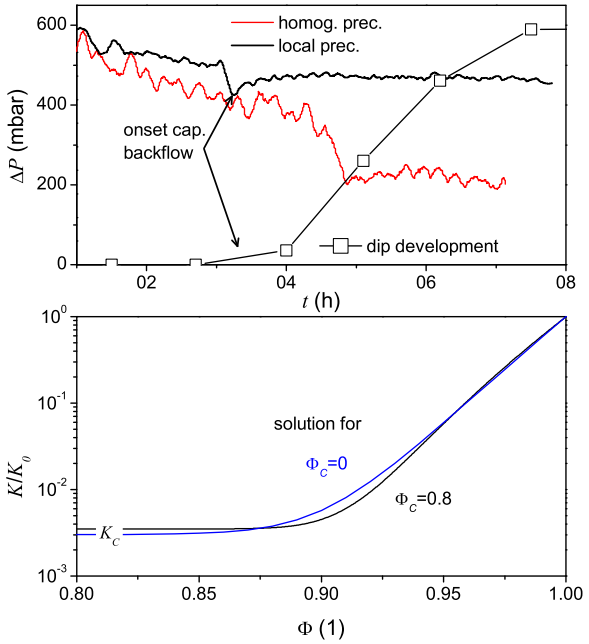

Fig. 8. Top: Pressure drop ΔP over the core during CO_2 injection. Two cases are shown: (1) the local precipitation case as discussed in the text (black line), and (2) ΔP recorded during homogeneous precipitation for comparison (red line). The open symbols represent the development of the local precipitate (salt saturation in arbitrary units) in Fig. 3. Bottom: $K(\Phi)$ relationships describing the experimental observations.

Please cite this article in press as: Ott, H., et al., Salt precipitation due to supercritical gas injection: I. Capillary-driven flow in unimodal sandstone. Int. J. Greenhouse Gas Control (2015), http://dx.doi.org/10.1016/j.ijggc.2015.01.005

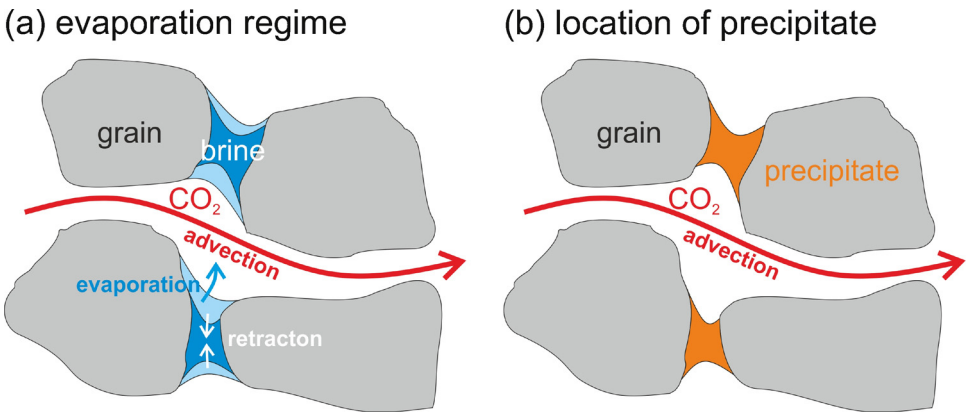

Fig. 9. Schematic view on the dry-out and precipitation process. (a) Retraction of the brine phase (menisci) due to evaporation leading to an increase of CO_2 relative permeability. (b) The precipitate is essentially located in the volume formerly occupied by the brine phase.

(with the exponent fitted to the data) as shown in the lower panel of Fig. 8 such that either result can be used for a practical purpose in the relevant porosity range $\Phi = \phi/\phi_0 = 1$ to 0.8. As we will argue below, the maximum salt saturation is equal to the residual brine saturation ($S_{salt,\max} = S_{W,res}$) and therefore $\Phi_C = 1 - S_{W,res} = 0.8$. With this we are able to determine the remaining fitting parameter τ, resulting in the parameter set: $K_C/K_0 = 3.5 \times 10^{-3}$, $\Phi_C = 0.8$ and $\tau = 10.1$.

K_C is likely to be a result of the observed precipitation pattern as shown in Fig. 7a–e. The images shows μCT cross sections (top row) and a 3D image of the data already presented in Fig. 3 and were recorded with 24 μm voxel size (pseudo pore-scale resolution), which is a compromise between spatial resolution and a proper field of view with an improved time resolution (shorter total scanning time). The images range from close to the inlet (a) to about 0.5 cm into the sample (e) and show the solid-salt contribution of the dry sample. Conspicuously, the salt precipitates in spots on different length scales, ranging from a mm-scale to a sub-mm or even a micrometer-scale. A 3D representation of the solid salt distribution is shown in the lower part of Fig. 7 in orange, while the early CO_2 percolation pattern is given in the right front corner of the 3D graph in blue. Both patterns occupy complementary space and overlap by less than 5 % of the common cross section. This indicates that salt precipitates in the vicinity of the initially CO_2 occupied volume, leaving the initial CO_2-pathways essentially open.

The data presented so far together with a couple of simple arguments allow us to construct a mind model – illustrated in Fig. 9 – that supports and summarizes the findings of this work:

1. Viscous brine displacement and water evaporation act in parallel, but were found to be dominant on different time scales. While residual brine saturation is usually reached after injection of a few pore volumes, complete dry-out was reached after hundreds of pore volumes of injected CO_2. There is essentially no viscous brine displacement during dry-out.
2. The structure of the residually trapped brine phase is determined by capillary forces.
3. After reaching the solubility limit, salt precipitates in the brine phase, and hence in the volume occupied by the residual brine, $S_{W,res}$.
4. The brine-saturated volume retracts during evaporation, leaving the precipitated salt behind.
5. There is no transport mechanism of liquid water vapor across the CO_2–brine interface and hence no transport mechanism of salt into the into the CO_2 flow channels – the flow channels serve for water vapor transport, but stay open since salt precipitates in the residual brine phase.

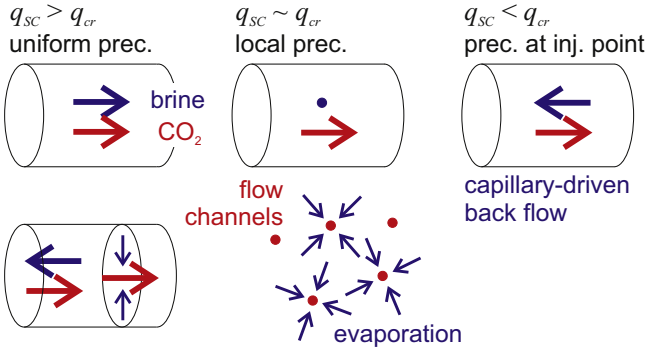

Fig. 10. Top row: schematic view of the different flow regimes that determine the precipitation pattern and are characterized by the flow rate with respect to a critical flow rate q_{cr}. Bottom row: schematic cross-sectional capillary-driven brine transport as described in the text.

6. Because of the well separated time scales of viscous displacement and evaporation, the maximum pore volume that can be filled by precipitate is the volume corresponding to the residual brine saturation, $S_{W,res}$. We conclude: $S_{salt,\max} = S_{W,res}$. In Berea sandstone we typically find $S_{W,res} \approx 0.2$, which corresponds to the maximum observed salt accumulation in the present study.

7. Summary and conclusions

In summary, we investigated consequences of dry-zone formation in the vicinity of gas injection and production wells. In core flood experiments we injected dry SC CO_2 into brine-saturated sandstone samples and reached complete dry-out. During the floods we measured effective permeability and fluid and salt saturations.

We found that time scales of viscous displacement and drying are practically well separates. Two mechanisms turned out to be of importance: (1) macroscopic solute transport due to capillary pressure gradients, which determines the macroscopic salt distribution, and (2) the pore-scale arrangement of fluid phases during viscous displacement and the drying process. Such local effects determine effective permeability, the porosity–permeability relationship and probably the maximum possible saturation of salt in the pore space.

The principal mechanism of solute transport and the condition under which local precipitation occurs have been investigated by experiments and numerical simulations. The results are schematically displayed in Fig. 10. We identified the origin of a critical flow rate above which salt precipitates homogeneously on a macroscopic scale. Below the critical flow rate, capillary-induced back

Please cite this article in press as: Ott, H., et al., Salt precipitation due to supercritical gas injection: I. Capillary-driven flow in unimodal sandstone. Int. J. Greenhouse Gas Control (2015), http://dx.doi.org/10.1016/j.ijggc.2015.01.005

flow of the remaining brine phase transports solutes in the direction of the injection point, where salt eventually precipitates. We further identified the length scale over which solutes can potentially be transported as a function of injection rate. The zone of attraction has been found to be 0.4 m for the described experimental situation and can reach several meters depending on the flow rate. Due to counter current flow, the amount of precipitate per unit volume can exceed the volume of salt originally dissolved in the brine in the respective volume.

From the presented experiments we calculated the permeability–porosity relationship, $K(\phi)$, describing the effect of precipitation in sandstone under the respective flow conditions. Despite the observed strong reductions of absolute permeability, the effective CO_2 permeability increased during the experiment in all cases. This relatively mild impact of precipitation on the sample permeability can be attributed to the observed local precipitation pattern; salt precipitates in the brine phase and hence in the vicinity of CO_2-conducting channels, leaving these channels essentially open.

The results of the study are of direct relevance for the risk assessment of injection operations, and are of practical used for injectivity modeling. For the prediction of macroscopic salt transport and the resulting porosity reductions, injection rates and effective evaporation rates need to be taken into account. The dimension of the affected zone has been estimated to be in the order of several centimeters to meters, which is valuable input for an adequate gridding around gas injectors and producers in reservoir modeling. For similar rock types, the respective permeability reduction can be modeled by the obtained $K(\phi)$ relationship.

Salt precipitation in similar rock types will lead to an absolute-permeability reduction, but to an improving effective permeability during the injection process. For that reason, we expect a relatively mild impact of salt precipitation on injectivity compared to the case of multi-modal carbonates as investigated in a companion paper by Ott et al. (2014).

Acknowledgments

The authors thank Steffen Berg and Jeroen Snippe for fruitful discussions and for reviewing the manuscript. Fons Marcelis is acknowledged for sample characterization and preparation and Pacelli Zitha for continuous support and discussions.

References

Andre, L., Peyssona, Y., Azaroual, M., 2014. Well injectivity during CO_2 storage operations in deep saline aquifers: Part 2. Numerical simulations of drying, salt deposit mechanisms and role of capillary forces. Int. J. Greenh. Gas Control 22, 301–312.

Bacci, G., Korre, A., Durucan, S., 2011. Experimental investigation into salt precipitation during CO_2 injection in saline aquifers. Energy Procedia 4, 4450–4456.

Bachu, S., Gunter, W.D., 2004. Overview of acid–gas injection operations in Western Canada. In: Proceedings of the 7th International Conference on Greenhouse Gas Control Technologies, Vancouver, Canada, 5–9 September, 2004, vol. 1.

Berg, S., Oedai, S., Ott, H., 2013. Displacement and mass transfer between saturated and unsaturated CO_2–brine systems in sandstone. Int. J. Greenh. Gas Control 12, 478–492.

Ehrenberg, S.N., Nadeau, P.H., 2005. Sandstone vs. carbonate petroleum reservoirs: a global perspective on porosity-depth and porosity–permeability relationships. AAPG Bull. 89 (4), 435–445.

Giorgis, T., Carpita, M., Battistelli, A., 2007. 2D modeling of salt precipitation during the injection of dry CO_2 in a depleted gas reservoir. Energy Convers. Manag. 48, 1816–1826.

Hubbell, J.H., 1969. Photon Cross Sections, Attenuation Coefficients, and Energy Absorption Coefficients From 10 keV to 100 GeV. Tech. Rep. NSRDS-NBS 29. U.S. Department of Commerce, National Bureau of Standards.

IPCC, 2005. IPCC Special Report on Carbon Dioxide Capture and Storage. Cambridge University Press, UK.

Kleinitz, W., Koehler, M., Dietzsch, G., 2001. The precipitation of salt in gas producing wells. Society of Petroleum Engineers SPE 68953, 1–7.

Lide, D.R., 2003. Handbook of Chemistry and Physics. CRC Press.

Ott, H., Berg, S., Oedai, S., 2011a. Displacement and mass transfer of CO_2/brine in sandstone. In: Society of Core Analysis Conference Paper SCA2011-05.

Ott, H., de Kloe, K., Marcelis, F., Makurat, A., 2011b. Injection of supercritical CO_2 in brine saturated sandstone: pattern formation during salt precipitation. Energy Procedia 4, 4425–4432.

Ott, H., de Kloe, K., Taberner, C., Marcelis, F., Wang, Y., Makurat, A., 2010. Rock/fluid interaction by injection of supercritical CO_2/H_2S: investigation of dry-zone formation near the injection well. In: Society of Core Analysis Conference Paper SCA2010-20.

Ott, H., de Kloe, K., van Bakel, M., Vos, F., van Pelt, A., Legerstee, P., Bauer, A., Eide, K., van der Linden, A., Berg, S.A.M., 2012. Core-flood experiment for transport of reactive fluids in rocks. Rev. Sci. Instrum. 83 (084501-1-084501-16).

Ott, H., Snippe, J., de Kloe, K., Husain, H., Abri, A., Makurat, A., 2014. Salt precipitation due to supercritical gas injection: II. Single vs. multi porosity rocks. Int. J. Greenh. Gas Control (submitted for publication).

Pape, H., Clauser, C., Iffland, J., 1999. Permeability prediction based on fractal pore-space geometry. Geophysics 64 (5), 1447–1460.

Perrin, J.-C., Benson, S., 2010. An experimental study on the influence of sub-core scale heterogeneities on CO_2 distribution in reservoir rocks. Trans. Porous Media 82, 93–109.

Peyssona, Y., Andre, L., Azaroual, M., 2014. Well injectivity during CO_2 storage operations in deep saline aquifers: Part 1. Experimental investigation of drying effects, salt precipitation and capillary forces. Int. J. Greenh. Gas Control 22, 291–300.

Pruess, K., García, J., 2002. Multiphase flow dynamics during CO_2 injection into saline aquifers. Environ. Geol. 42, 282–295.

Pruess, K., Müller, N., 2009. Formation dry-out from CO_2 injection into saline aquifers: 1. Effects of solids precipitation and their mitigation. Water Resour. Res. 45, W03402.

Pruess, K., Spycher, N., 2007. ECO2N – a fluid property module for the TOUGH2 code for studies of CO_2 storage in saline aquifers. Energy Convers. Manag. 48, 1761–1767.

Roels, S.M., Ott, H., Zitha, P.L.J., 2014. μ-CT analysis and numerical simulation of drying effects of CO_2 injection into brine-saturated porous media. Int. J. Greenh. Gas Control 27, 146–154.

Schutjens, P.M.T.M., Hanssen, T.H., Hettema, M.H.H., Merour, J., de Bree, P., Coremans, J.W.A.G.H., 2004. Compaction-induced porosity/permeability reduction in sandstone reservoirs: data and model for elasticity-dominated deformation. SPE Reserv. Eval. Eng. 7 (3), 202–216.

Span, R., Wagner, W., 1996. A new equation of state for carbon dioxide covering the fluid region from the triple-point temperature to 1100 k at pressures up to 800 mPa. J. Phys. Chem. Ref. Data 25 (6), 1509–1596.

Spycher, N., Pruess, K., 2005. CO_2–H_2O mixtures in the geological sequestration of CO_2: II. Partitioning in chloride brines at 12–100 °C and up to 600 bar. Geochim. Cosmochim. Acta 69 (13), 3309–3320.

van Genuchten, M.T., 1980. A closed-form equation for predicting the hydraulic conductivity of unsaturated soils. Soil Sci. Soc. Am. J. 44, 892–898.

Verma, A., Pruess, K., 1988. Thermohydrological conditions and silica redistribution near high-level nuclear wastes emplaced in saturated geological formations. J. Geophys. Res. 93, 1159–1173.

Vinegar, H.J., Wellington, S.L., 1987. Tomographic imaging of three-phase flow experiments. Rev. Sci. Instrum. 58 (1), 96–107.

Wellington, S.I., Vinegar, H.J., 1987. J. Petrol. Technol. SPE 16983, 885–898.

Wyble, D.O., 1958. Permeability prediction based on fractal pore-space geometry. Trans. Soc. Pet. Eng. AIME 213, 430–432.

Xu, T., Apps, J.A., Pruess, K., 2004a. Numerical simulation of CO_2 disposal by mineral trapping in deep aquifers. Appl. Geochem. 19, 917–936.

Xu, T., Ontoy, Y., Molling, P.N.S., Parini, M., Pruess, K., 2004b. Reactive transport modeling of injection well scaling and acidizing at Tiwi field, Philippines. Geothermics 33, 477–491.

Zuluaga, E., Monsalve, J.C., 2001. Water vaporization in gas reservoirs. Soc. Petrol. Eng. SPE 84829, 1–4.

Zuluaga, E., Muñoz, N.I., Obando, G.A., 2001. An experimental study to evaluate water vaporisation and formation damage caused by dry gas flow through porous media. Soc. Petrol. Eng. SPE 68335, 1–7.

Please cite this article in press as: Ott, H., et al., Salt precipitation due to supercritical gas injection: I. Capillary-driven flow in unimodal sandstone. Int. J. Greenhouse Gas Control (2015), http://dx.doi.org/10.1016/j.ijggc.2015.01.005